applied sciences

MDPI

Article

Multi-Modal X-ray Imaging and Analysis for Characterization of Urinary Stones

Somayeh Saghamanesh [1,*], Henning Richter [2], Antonia Neels [1,3] and Robert Zboray [1,*]

[1] Center for X-ray Analytics,Department Materials Meet Life, Swiss Federal Laboratories for Material Science and Technology, Empa, Überlandstrasse 129, 8600 Dübendorf, Switzerland; antonia.neels@empa.ch
[2] Diagnostic Imaging Research Unit (DIRU), Clinic for Diagnostic Imaging, Department of Clinical Diagnostics and Services, Vetsuisse Faculty, University of Zürich, Winterthurerstrasse 258c, 8057 Zürich, Switzerland; henning.richter@uzh.ch
[3] Department of Chemistry, University of Fribourg, Chemin du Musée 9, 1700 Fribourg, Switzerland
* Correspondence: somayeh.saghamanesh@empa.ch (S.S.); robert.zboray@empa.ch (R.Z.)

Abstract: Backgound: The composition of stones formed in the urinary tract plays an important role in their management over time. The most common imaging method for the non-invasive evaluation of urinary stones is radiography and computed tomography (CT). However, CT is not very sensitive, and cannot differentiate between all critical stone types. In this study, we propose the application, and evaluate the potential, of a multi-modal (or multi-contrast) X-ray imaging technique called speckle-based imaging (SBI) to differentiate between various types of urinary stones. Methods: Three different stone samples were extracted from animal and human urinary tracts and examined in a laboratory-based speckle tracking setup. The results were discussed based on an X-ray diffraction analysis and a comparison with X-ray microtomography and grating-based interferometry. Results: The stones were classified through compositional analysis by X-ray diffraction. The multi-contrast images obtained using the SBI method provided detailed information about the composition of various urinary stone types, and could differentiate between them. X-ray SBI could provide highly sensitive and high-resolution characterizations of different urinary stones in the radiography mode, comparable to those by grating interferometry. Conclusions: This investigation demonstrated the capability of the SBI technique for the non-invasive classification of urinary stones through radiography in a simple and cost-effective laboratory setting. This opens the possibility for further studies concerning full-field in vivo SBI for the clinical imaging of urinary stones.

Keywords: kidney stone; urinary stone; KUB radiography; X-ray computed tomography; X-ray speckle-based imaging; X-ray phase-contrast and dark-field imaging

Citation: Saghamanesh, S.; Richter, H.; Neels, A.; Zboray, R. Multi-Modal X-ray Imaging and Analysis for Characterization of Urinary Stones. *Appl. Sci.* **2022**, *12*, 3798. https://doi.org/10.3390/app12083798

Academic Editor: Thomas Schmid

Received: 10 March 2022
Accepted: 7 April 2022
Published: 9 April 2022

1. Introduction

Kidney stone diseases (nephrolithiasis) and urinary stones diseases (urolithiasis) affect about 5% of the global population [1]. A high prevalence of these widespread diseases, with increasing rates in both infants and adults, is observed especially in industrialized countries with high socio-economical standards. Knowledge of the composition of urinary tract stones is a fundamental part of the preoperative patient evaluation, and this information influences treatment plans and recurrence prevention [2,3]. Twenty-four-hour urine collection, used to measure key components in the urine, is the most common method to assess urinary stone risk factors. For example, calcium oxalate (CaOx) stones can form under a wide range of physiological urinary pH conditions, while hydroxylapatite (HA) stones tend to form in alkaline urine [4]. Urinary supersaturation (SS), calculated from the composition of a twenty-four-hour urine collection, also correlates with the crystalline component of the stones passed. Therefore, physicians rely largely on the urine pH and urine SS profile to predict the stone composition [4], but the prediction capability of this method alone is mostly insufficient.

The standard imaging methods for the diagnosis and evaluation of urinary stones are ultrasonography (US), kidney–ureter–bladder (KUB) radiography, and non-contrast-enhanced computed tomography (NCCT) of the abdomen and pelvis [5,6]. US is widely accessible and poses no radiation dose, but suffers from low sensitivity and specificity. For X-ray imaging, one challenge is that only 60% of all renal stones are radiopaque and bear no risk of being missed [5,6]. Recently, dual-energy CT (DECT) has been suggested to improve the prediction capability for stone-type differentiation, compared to the standard CT [3–6]. By facilitating low- and high-energy scanning during a single acquisition, DECT has the inherent capability to help differentiate between materials that have similar electron densities but varying photon absorptions [3–5]. DECT is nearly 100% accurate when characterizing uric acid (UA) stones, both in vitro and in vivo [4]. Recently, some progress has been made to differentiate between non-UA stone types, such as calcium oxalate and hydroxlyapatite stones [7]. However, the ability of DECT to discriminate among stone types depends on the difference between the CT number ratio of the materials, which is determined by the difference in the atomic numbers of stone components and the spectral separation [7]. The effective atomic numbers of the UA stone types fall into a narrow range (6.84–7.01); the effective atomic numbers of non-UA stones are higher and more varied (10.78–15.56). The large difference in the effective atomic numbers of UA and non-UA stones explains the ability of DECT to differentiate UA from non-UA stones with higher accuracy. However, the differences in the effective atomic numbers among the common non-UA stones such as cystine, struvite, calcium oxalate, brushite, and apatite are much smaller. Considering that many stones are a combination of two or more of the above compositions, a true differentiation of various stones remains a great challenge [7].

Multi-modal X-ray imaging techniques can potentially be an alternative for urinary stone diagnosis. These imaging techniques are sensitive to small phase shifts of X-ray wave fronts upon their interaction with matter, in addition to the amplitude attenuation; hence, they can provide additional contrast channels, such as phase-contrast and dark-field channels, that reveal complementary information about the inner microstructures [8,9]. The phase shift occurs due to the refraction of X-rays inside the matter and is considered the coherent effect of X-ray diffraction from the sample. The dark-field contrast is generated due to the ultra-small-angle scattering of X-rays from structures of a sub-pixel-length scale, which results in a diffused beam and reduced visibility of the recorded intensity, typically with respect to a empty-field reference image [10–13].

Many versatile applications have been demonstrated for X-ray phase-sensitive methods during the last two decades, from material characterization [14–18] to biomedical virtual 3D histology [19–26]. Various operational mechanisms have been implemented to extract such multi-contrast images by changing the configuration of X-ray radiography and tomography systems or introducing some optical elements [27]. Furthermore, most of them require a high degree of temporal and spatial beam coherence to provide efficient imaging. Therefore, most of them have been realized in synchrotron facilities. However, some of these techniques can be implemented with laboratory sources such as propagation-based imaging (PBI) [28], grating-based interferometry (GI) [29], edge-illumination imaging (EI) [30], and speckle-based imaging (SBI) [31,32].

The differentiation of urinary stone types through dark-field imaging has been investigated by Scherer et al. [33] with the GI technique. The authors provided a classification based on the complementarity of the absorption and dark-field contrast images. Since scattering mainly takes place at boundaries with locally changing densities and rich and varying microstructures, the resulting scattering signal is strong, whereas homogeneous and less micro-structured compositions lead to smaller scattering intensities [33–35]. On the other hand, the relation is the opposite for the absorption intensities. It has been shown, for in vitro urinary stones, that the ratio of the scatter and absorption coefficient can be used as an indicator of the stone type [33,35]. The sensitivity and specificity of the GI method, based on these preliminary results, seem to be excellent, superseding those based solely on absorption imaging (i.e., CT and DECT).

However, the GI method has some limitations that makes its use for actual clinical applications challenging. First of all, the GI technique relies on the micro-structured absorption gratings which, despite other grating-based methods such as EI [36], need to be fabricated in high aspect ratios. Therefore, the gratings are currently difficult and expensive to make for high-energy full-field imaging such as pelvis and abdomen imaging. Moreover, GI needs an additional source grating in order to be used with high-power X-ray sources and to provide a sufficient spatial coherence. This would impose a beam flux loss and suboptimal photon economy [36] and, consequently, an extra delivered dose to the pelvis and abdomen upon increasing the exposure time for achieving a sufficient signal-to-noise ratio (SNR). The time is also lengthened by a phase-scanning procedure, which is necessary to measure the interference modulation that further increases the scanning time and absorbed radiation dose.

Another multi-modal technique is speckle-based imaging (SBI) [37], of which a schematic is provided in Figure 1. The main advantage of this technique is simplicity and cost-effectiveness, with low coherence requirements (see Section 2.1). This method allows multimodal imaging at high energies and with a large field of view (FOV), with essentially no stepping procedure with laboratory sources. This has great potential for studying laboratory-based SBI for many medical applications [23,38].

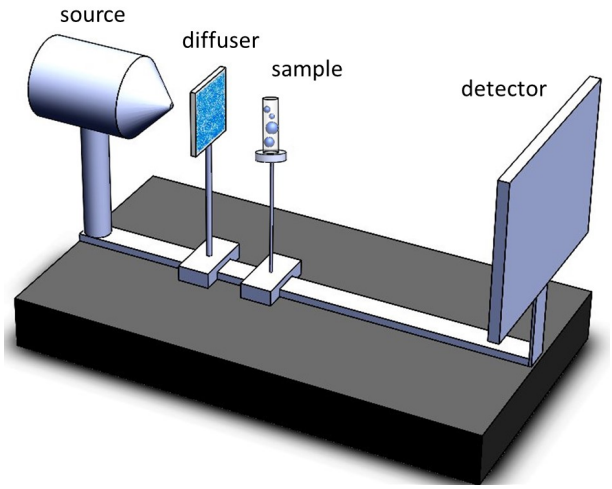

Figure 1. Depiction of the experimental setup for the X-ray speckle tracking imaging.

In this work, we present an ex vivo multi-modal evaluation of different urinary stone types through the X-ray speckle-based imaging technique as a new technical approach to the problem. We confirm and compare our findings with X-ray diffraction (XRD), volumetric analysis by microtomography, and the GI technique. We will specifically discuss the potential of SBI in regards to the characterization and classification of urinary stones, and also regarding its potential for in vivo applications.

2. Materials and Methods

The sample collection of this study included urolithiasis from different species. One sample each from a dog, cat, and human was collected as surplus from laboratory analysis, based on the written consent forms for research use of samples. All samples were examined with X-ray speckle-based imaging (SBI), X-ray microtomography, X-ray grating-based interferometry (GI), and X-ray diffraction (XRD).

2.1. X-ray Speckle-Based Imaging (SBI)

A typical experimental configuration of speckle-based imaging is depicted in Figure 1. The system is basically similar to a conventional X-ray radiography and tomography, except for a random-pattern diffuser which is placed upstream or downstream of the sample. The diffuser modulates the partially coherent X-ray wave front by creating random speckles

on the detector. The speckle pattern can be used as a wave marker to detect any phase shifts and scattering from the sample by displacing the speckles, compared with a reference image without the sample. The system can operate with only two projections, a sample and a reference; such a sustem is then called X-ray speckle tracking (XST). However, one can scan the diffuser along one or two orthogonal directions to increase the spatial resolution when unraveling the speckle modulation [39].

Radiography images were acquired from three stone samples in an XST-SBI setup. The system was implemented with a Hamamatsu L10801 X-ray tube operated at 80–100 kVp and 1.5–2 mAs with 10 average frames. The source was placed 100 cm from a digital flat-panel detector, consisting of a 700 µm-thick CsI-scintillator layer. The detector elements were arranged in 1496 × 1880 pixels with 127 µm width. A sandpaper sheet with an average grit size of 18 µm was used as the diffuser. Two images were acquired from each sample, one with the diffuser and the sample and one without the sample. The images were analyzed in MATLAB to retrieve the multimodal signals. For the phase-contrast images, an implicit speckle tracking method was employed to extract the average refraction angles along two orthogonal directions [40]:

$$\alpha_{x(y)} = \frac{1}{k}\frac{\partial}{\partial x(y)}\left[\frac{1}{\mu} log_e F^{-1}\left(LFF\left(\frac{F[1 - I(x,y)/I_0(x,y)]}{1 + \pi\gamma D\lambda(u_x^2 + u_y^2)}\right)\right]\right. \quad (1)$$

where γ is $\frac{\delta}{\beta}$, for which δ and β are the real and imaginary parts of the complex refractive index of X-rays at the mean X-ray energy. In addition, μ is the linear attenuation coefficient, D is the propagation distance, λ is the X-ray wavelength, and (u_x, u_y) are the spatial frequency components in the Fourier space, corresponding to (x, y) in the image space. F and F^{-1} are the Fourier and the inverse Fourier transform, respectively. LFF is an optional low-frequency filter applied in the Fourier space to eliminate the effect of low-frequency random noise introduced when retrieving the phase. The pure attenuation image (T) is obtained by:

$$T(x_i, y_j) = \frac{\overline{I}(x', y')}{\overline{I_0}(x, y)} \quad (2)$$

where $\overline{I_0}(x, y)$ describes the mean reference signal value in a 15 × 15 sliding analysis window with a central pixel at (x_i, y_j). As such, the modulated $\overline{I}(x', y')$ is the mean intensity value centered at (x_i, y_j). The dark-field (D) image implies the diffusion of partially coherent X-rays inside the sample, calculated as:

$$D(x_i, y_j) = \frac{1}{T(x_i, y_j)}\frac{\sigma}{\sigma_0} \quad (3)$$

where σ_0 and σ are the standard deviations of the reference and the sample images in the subset window, respectively.

2.2. X-ray Microtomography

The samples were scanned in a normal tomography setup in the EasyTom XL Ultra 160 (RX Solution) micro/nanoCT scanner. X-ray micro tomography alone can provide a 3D visualization of internal micro-structures, as indicated by changes in the X-ray attenuation value of the stones. The microfocus source with an additional 0.35 mm-thick copper filter was operated at 140 kVp and in the range of 25–360 µAs. The detector was a digital flat-panel detector with a CsI scintillator with a pixel size of 127 µm. The projection images were then processed and reconstructed through Xact software (revision 21.04), and 3D volume images were analyzed and visualized by VGStudio MAX 3.3 software.

2.3. X-ray Grating-Based Interferometry (GI)

An in-house X-ray Talbot–Lau grating interferometry setup was also employed to acquire multi-contrast images from three urinary stone samples. The interferometer con-

sisted of a Varian HPX 160-11 conventional source, a Teledyne Dalsa Shad'o'Box flat-panel detector with Gadox scintillator, and three line gratings made by KIT Microworks. The source grating G0 was made of multiple 70 µm-high gold lines etched into a Si wafer with a 30 µm pitch and 0.3 duty cycle. The G0 creates partially coherent beams from the incoherent X-ray tube, working at 45 kVp and 20 mA. The phase grating G1 had multiple 2.92 µm-pitch line patterns with a 6.1 µm nickel depth. This grating creates a periodic wave pattern, generating interference fringes at the 4th Talbot distance on the absorption grating G2. The grating G2 was made of multiple 70 µm-high gold lines etched into a Si wafer with a period of 3.24 µm. The G0 to G1 and G1 to G2 distances were 1238 mm and 134 mm, respectively. The detector pixel size was 49.5 µm [35].

The three samples were scanned through an 11-step scanning process over one G2 period, and the same process was performed without the sample to obtain the reference images. Each frame was acquired in 2.2 s, which, in total, took 50 s for the whole image acquisition for each sample. The fringe intensity modulation was recorded and analyzed through a common Fourier analysis in a built-in MATLAB program at Empa to retrieve three attenuation, differential phase-contrast, and dark-field images from the interferometer.

2.4. X-ray Diffraction (XRD)

The XRD analysis was used here as the reference standard for stone composition analysis. To determine the structure of poly/single crystalline compounds of the three urinary stone samples, a small piece of stone samples was cut and examined using XRD methods. Two-dimensional wide-angle X-ray diffraction (2D-WAXD) was performed on a STOE IPDS-II, using Mo-K_α radiation (0.71073 Å) at 40 mA, 50 kVp for 30 min with a beam diameter of 500 µm in the transmission mode. The sample was placed perpendicular to the beam to allow the X-rays to pass through the sample. The WAXD patterns were recorded on an image-plate detector system with a 340 mm diameter placed at a distance of 200 mm from the sample. The diffraction images were recorded covering a 2Θ range from 1.3° to 40°. For the phase analysis, 1D scans were obtained through a 360° radial integration of the 2D images.

While the IPDS-II detection system allows for the study of the overall structural state of the samples (crystallinity, ordering), it is limited in resolution. With highly crystalline samples, for a better peak separation and indexing, a PANalytical X'Pert Powder instrument was used in a Bragg–Brentano configuration on powder samples. Data was collected at room temperature using Cu-K_α radiation (λ = 1.5406 Å). The phase analysis was carried out using the program Highscore Plus from Malvern Panalytical [41].

3. Results

3.1. X-ray Diffraction

The 2D diffraction images from the XRD measurements from the STOE-IPDS instrument are shown in Figure 2a–c) for the three investigated samples. They allow for differentiating between the exciting structural features with respect to the phases, crystallinity, and orientation. The dog sample shows the highest crystallinity based on the observed single crystal diffraction behavior, which is clearly seen through the diffraction spots on the 2D detector. The cat sample reveals a random orientation of crystallites. This is monitored through sharp rings on the 2D images, also indicating a high crystallinity and exceeding the detector resolution. The human sample is clearly nano- and polycrystalline, which is seen by broader diffraction rings compared to the cat sample. The 1D diffraction patterns for these three samples were produced from a powder, and are presented in Figure 2d. The results of the phase analysis are presented, respectively, in Table 1. It should be recalled that the analysis was conducted for a piece of the stone samples, so the information regarding the "main" and "minor" assignment does not necessarily represent the whole stone, but the outer part of the sample.

From Figure 2, it can be seen that very different crystallographic phases are found in the extracted mineralizations. Detailed phase analyses are illustrated in Figure A1 of the Appendix. While, from the cat and human samples, mostly calcium oxalate and phosphate compounds are identified, the dog sample shows a single crystalline magnesium phosphate in its struvite form (see Table 1 and Figure A1). Struvite is a normal component of dog's urine and will remain dissolved as long as the struvite concentration is low and the urine is acidic. Higher concentrations and alkaline urine result in stone formation. The cat sample reveals mainly hydroxyapatite and whewellite as a minor phase. In the human sample, only calcium phosphate components were identified—hydroxyapatite, as the main phase, and whitelockite as the minor phase. Details on phase formations are given in Table 1. Figure 2d reveals a strong increase of crystallinity from the human to the cat, then to the dog sample. Crystallinity evaluates the crystalline (well-resolved reflections) relative to the amorphous (background) part of the sample. The dog sample shows single crystalline behavior, which would be an indication of the slow growth of the entire stone.

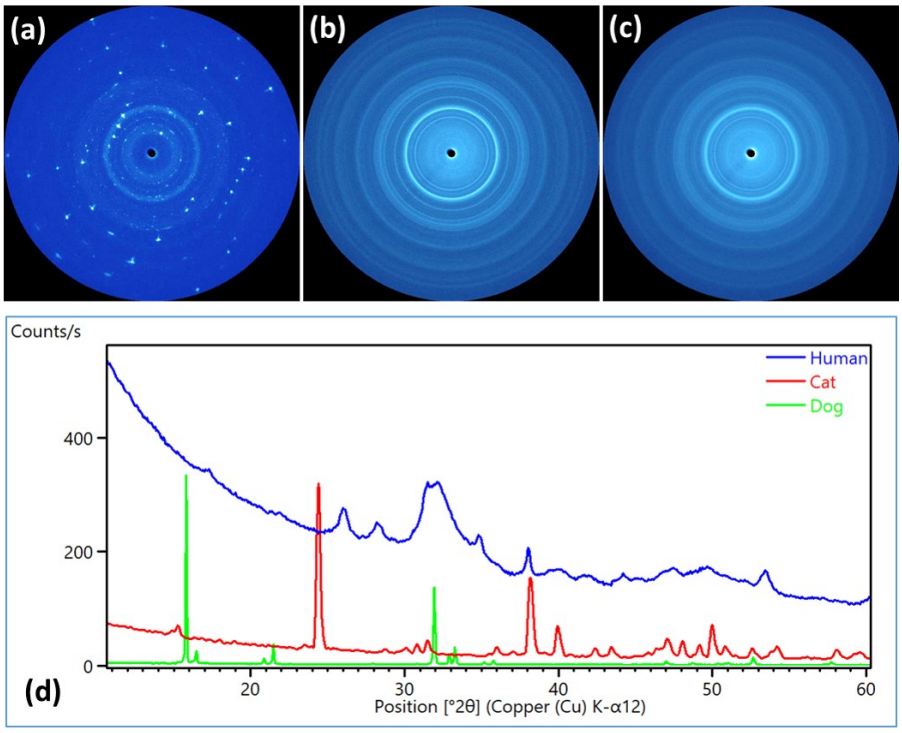

Figure 2. The 2D diffraction patterns of the stone samples from (**a**) dog, (**b**) cat, and (**c**) human urinary stone samples. (**d**) The 1D diffraction profiles of the three stones.

We see a clear difference in the type of phase formation and the crystalline state, both of which will affect the disease treatment.

Table 1. Composition and phase analysis of urinary stones by the XRD method.

Sample	Analysis	Chemical Formula	Crystal System	Space Group	Density (g/cm3)
Dog (SC) [1]	Struvite	$Mg(NH_4)(PO_4)\cdot 6H_2O$	Orthorhombic	$Pmn2_1$	1.7 (white)
Cat (poly) [2]	Whewellite (minor)	$Ca(C_2O_4)\cdot H_2O$	Monoclinic	$P2_1/n$	2.2 (brown-gray)
	Hydroxylapatite (main)	$Ca_5(PO_4)_3(OH)$	Hexagonal	$P6_3/m$	3.8 (gray-white)
Human (nano-poly) [3]	Whitelockite (minor)	$Ca_9(Mg,Fe)(PO_4)_6(PO_3OH)$	Tringonal	R3c	3.1 (gray-white)
	Hydroxylapatite (main)	$Ca_5(PO_4)_3(OH)$	Hexagonal	$P6_3/m$	3.8

[1] SC: single-crystal; [2] poly: polycrystalline; [3] nano-poly: nano-polycrystalline.

3.2. MicroCT Volumetric Analysis

Figure 3 shows reconstructed slices for each stone sample. A 3D rendering of the samples is also depicted in Figure 3.

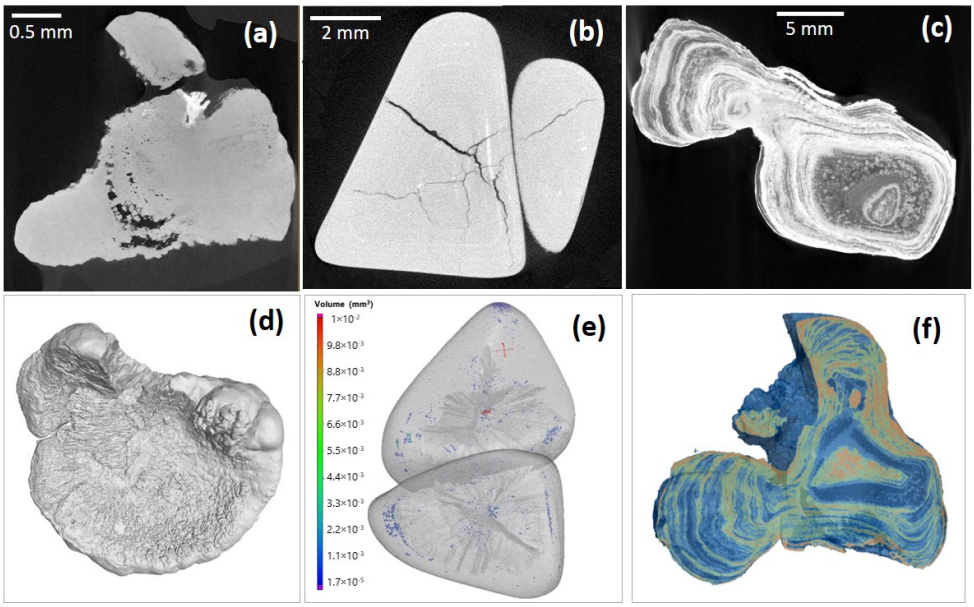

Figure 3. Reconstructed vertical slice of X-ray microtomography through three stone samples from (**a**) cat, (**b**) dog, and (**c**) human urinary stones. (**d**–**f**) Corresponding 3D rendering of the full stones in (**a**–**c**). In (**e**), the porosity size distribution is depicted by the side colorbar. The effective voxel sizes for the (**a**–**c**) microtomographs are 5.15, 12.86, and 39.9 μm, respectively.

The stone sample from the cat exhibits two main intensity ranges in the slice's histogram: a relatively medium intensity, uniformly distributed inside the stone, and some hyperintense regions mostly in central slices close to the border in one view. The lower-intensity area is detected to be polycrystalline whewellite, and the hyperintense signal at the core of the stone is related to the highly absorbing hydroxylapatite (Figure 3a). Some porosity and cracks can be visualized inside the stone. The stone surface shows considerable overall roughness and irregularities, seen in the edges of the reconstructed slices and well rendered in the 3D volume (Figure 3d).

The dog's stone appears very smooth in intensity, with some inner cracks and porosity, depicted in the image volume in Figure 3b,e. It is expected to see such a high degree of

intensity uniformity due to the single crystalline phase of this stone, detected by XRD analysis. The laminar structures of the human urinary stone can be well observed from the microCT slices, implying whitelockite as the repeated hyperintense layers grown around the relatively hypointense hydroxylapatite as the core (Figure 3c). There are granular heterogeneities from grown nano-polychrystalline whitelockite also distributed close and around the core. The hydroxyapatite layers are also observed between the whitelockite layers, creating high-contrast wavy patterns in the stone's cross-sections. It should be noted that the advantage of microCT is that it can provide high-resolution, full volumetric information of the stones.

3.3. X-ray Speckle-Based IMAGING (SBI)

Figure 4 represents the multi-modal radiographs retrieved from the XST-SBI technique for three stone samples.

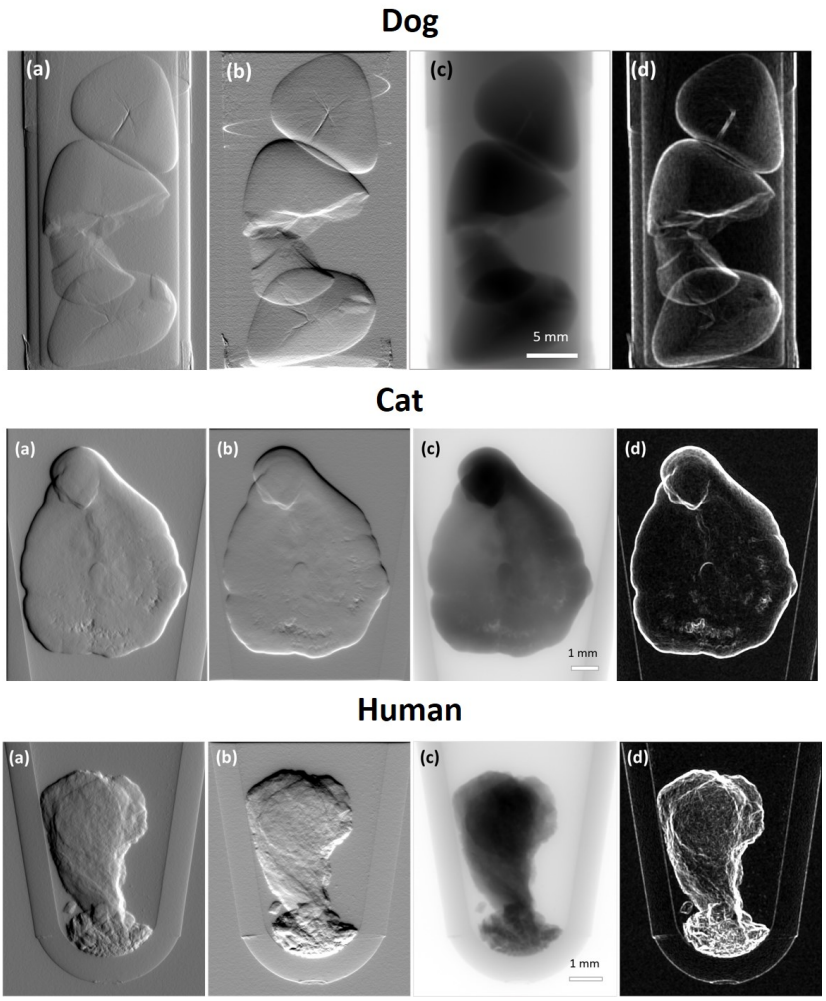

Figure 4. Multi-contrast radiographs extracted from dog, cat, and human urinary stones. (**a**) Horizontal refraction angle, (**b**) vertical refraction angle, (**c**) attenuation, and (**d**) dark-field contrast.

As observed from Figure 4, in all cases, the phase-contrast and dark-field images can provide more details about the heterogeneity, porosity, and roughness of the stone structure, added to the density and absorption information provided by the attenuation images. The dog's stone appears very smooth in structure in the attenuation and refraction images, except for some larger central cracks and porosity visible in the refraction images, as also observed in the microCT slices. However, the dark-field image of this sample additionally shows high-frequency signals related to the micro-porosities or large imperfections inside the crystalline stone, which can not be observed in the other two contrast images.

Generally, the dark-field radiographs reveal a high signal from the microstructurs and micro-porosities inside the urinary stones, due to the strong X-ray scattering from them (Figure 4d). Such micro-heterogeneities are below the spatial resolution of the imaging system and can not be visualized in the attenuation or refraction images. The strongest dark-field signals are observed for the human stone, which was known to have a layered and very non-uniform structure (Figure 4d—bottom). This heterogeneity can be also observed through the refraction images of the human stone as high-frequency refraction signals (Figure 4a,b—bottom). The cat's stone shows some degree of irregularity and porosity in some areas, which has generated strong signals both in refraction and dark-field images, as confirmed by microCT images to be mostly surface roughness. Other than this, the cat's stone exhibits more uniformity in the multi-contrast radiographs than the human sample.

3.4. X-ray Grating-Based Interferometry (GI)

The results of the Talbot–Lau grating interferometry for the dog, cat, and human urinary stones are shown in Figure 5. Here also, in all cases, the fine microstructures unraveled by the phase and dark-field contrast channels supersedes the attenuation radiographs. The superimposed layered structure of the human stone has also appeared as a high-frequency positive/minus differential phase signal (Figure 5c—bottom).

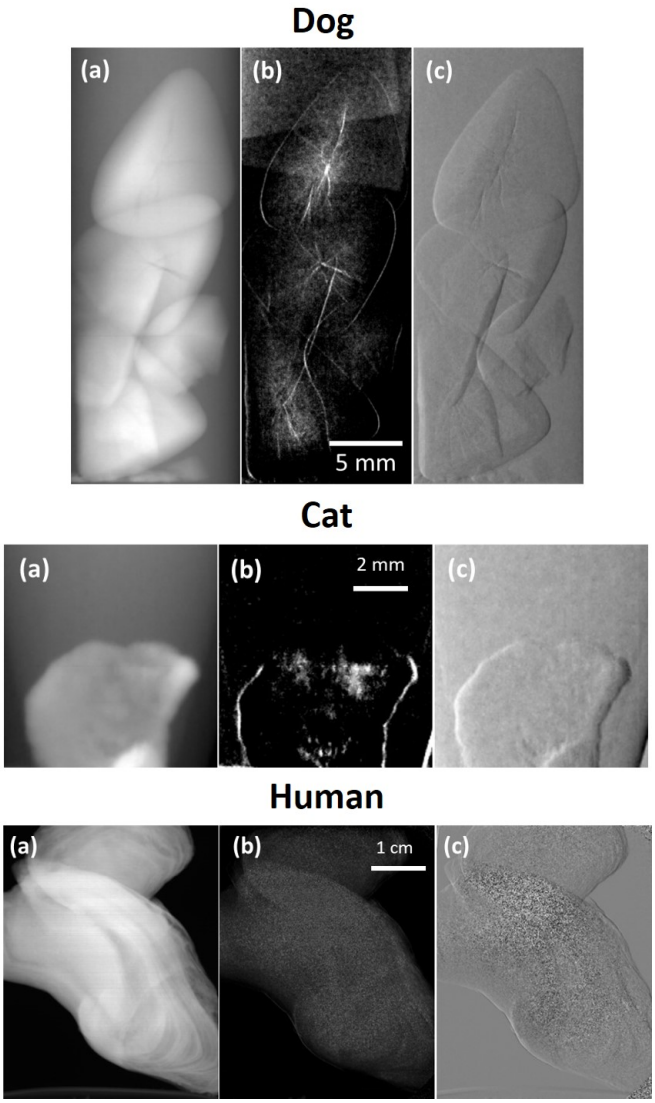

Figure 5. Retrieved (**a**) attenuation, (**b**) differential phase, and (**c**) dark-field images of three urinary stone samples taken by GI on the Talbot–Lau interferometer

4. Discussion

About 80% of stones are composed of calcium oxalate (CaC_2O_4) and/or hydroxyapatite [5]. The three state-of-the-art reference techniques for precise urinary tract stone analysis are all in vitro methods, including X-ray diffraction (XRD), infrared spectroscopy, and polarization microscopy [3]. These methods are not only costly and time consuming, as is the SS method, but they also have a major disadvantage in the sense that the composition analysis of the stones is performed only after the stones are extracted. Thus, they offer no benefit during the preoperative treatment planning. Therefore, a reliable, non-invasive, pre-intervention method for stone analysis would be of extreme benefit, as it could significantly decrease the necessity of surgical interventions and, in general, would improve patient-specific treatment planning.

Clinical CT, due to its low resolution compared to the high-resolution microCT, can not provide sufficient differentiation among all urinary stones. Moreover, it imposes much higher doses to the tissue than radiography. Hence, being able to provide accurate differentiation through a simple radiography would be an extra advantage, and would likely alleviate patient dose concerns. Therefore, X-ray phase-contrast and dark-field radiography could be a potential alternative to bring added values to the diagnosis of urinary stones. X-ray SBI of sample stones resulted in informative details about material heterogeneity and porosity at sub-pixel-resolution scales, and could differentiate between investigated stone types, i.e., struvite, polycrystalline mixed calcium oxalate-phosphate, and more heterogeneous nano-polycrystalline calcium phosphate phases. As explained in the introduction, following Scherer et al. [33], we have evaluated the distribution of the pixel-wise ratio of the absorption and dark-field images obtained by SBI. These clearly cluster around well-defined mean values, as is indicated in Table 2. These clearly different mean values, which are obtained over the full stone volume, can be used as indicators of the given stone type. The relatively high standard deviations of the distribution around the mean values are due to the heterogeneity of the full samples, as is illustrated by microtomography above. Note that the values of the absorption to the dark-field ratio using the SBI and GI methods on two completely different setups are not comparable due to, e.g., the different dark-field sensitivities of the different methods and setups (among other things), as is described by a setup-specific proportionality constant for the dark field in [33].

Table 2. Mean and standard deviation of the distribution of the pixel-wise absorption to the dark-field image gray-value ratio, a dimensionless quantity, taken over different stones types obtained by SBI.

Value	Cat	Dog	Human
mean	16.5	8.6	3.0
stdev	11.0	6.5	2.4

Due to its technical simplicity and the very high photon efficiency compared to X-ray GI, X-ray SBI bears the potential to be applied for non-invasive, in vivo human urinary stone classification and differentiation. To this end, further phantom and/or in vivo studies should be performed with a larger number of samples to extract texture features from multi-contrast images and to clarify the dose levels needed in realistic or in vivo settings to obtain reliable stone classification. For this, the simulation of in vivo imaging conditions by embedding stones in different combinations of cadaveric animal tissue, bladder, urine, etc., will be considered. This will be the topic of future research.

5. Conclusions

In this study, we have proposed and evaluated the potential of X-ray speckle-based imaging for the differentiation and classification of urinary stones. Three stones—one each from a human, a cat, and a dog—have been used to demonstrate the potential of the technique for classifying urinary stones. X-ray refraction and dark-field images were extracted from a laboratory implementation of an X-ray speckle tracking system in a fast radiogra-

phy. The SBI results were confirmed and discussed through compound analysis by XRD and volumetric data obtained from microCT and by multi-modal images from a grating-based setup. The multi-contrast images could reveal important details of the internal macro/micro-porosity and heterogeneity level, leading to distinctions between the urinary stones. In particular, dark-field imaging can detect the existence of sub-pixel-resolution structures, which could be valuable for differentiating various stone compositions and complementing the insufficient spatial resolution of clinical CT. This promotes further studies on the feature analysis of all existing stone types to provide a systematic classification of urinary stones in multi-modal speckle-based radiography/tomography. The simplicity and photon efficiency of SBI implementation, also at higher energies, promises its potential applicability in a full-field in vivo imaging setting.

Author Contributions: Conceptualization, S.S., H.R. and R.Z.; methodology, S.S., A.N. and R.Z.; samples, H.R.; software, S.S.; validation, S.S., A.N. and R.Z.; formal analysis, S.S., A.N. and R.Z.; investigation, S.S., A.N. and R.Z.; resources, H.R., S.S., A.N. and R.Z.; data curation, S.S., A.N. and R.Z.; writing—original draft preparation, S.S.; writing—review and editing, all authors; visualization, S.S., A.N. and R.Z.; supervision, S.S. and R.Z.; project administration, S.S., A.N. and R.Z.; funding acquisition, S.S., A.N. and R.Z. All authors have read and agreed to the published version of the manuscript.

Funding: This research was funded by the EMPA POSTDOCS-II programme, planned by the European Union's Horizon 2020 research and innovation program under the Marie Skłodowska-Curie grant agreement number 754364.

Institutional Review Board Statement: The study was conducted according to the guidelines of the Declaration of Helsinki, and approved by the Institutional Review Board of University of Zurich. Animal and human urinary stones were collected as surplus from laboratory analysis, based on written consent forms for research use of samples.

Informed Consent Statement: Animal and human urinary stones were collected as surplus from laboratory analysis, based on written consent forms for research use of samples.

Data Availability Statement: Data is contained within the article.

Acknowledgments: The authors would like to thank Alexander Flisch at Empa for providing a fixation holder arm for the experiments.

Conflicts of Interest: The authors declare no conflict of interest. The funders had no role in the design of the study; in the collection, analyses, or interpretation of data; in the writing of the manuscript, or in the decision to publish the results.

Abbreviations

The following abbreviations are used in this manuscript:

CT	Computed tomography
DECT	Dual-energy computed tomography
EI	Edge-illumination
GI	Grating-based interferometry
SBI	Speckle-based imaging
WAXD	Wide-angle X-ray diffraction
XRD	X-ray diffraction

Appendix A

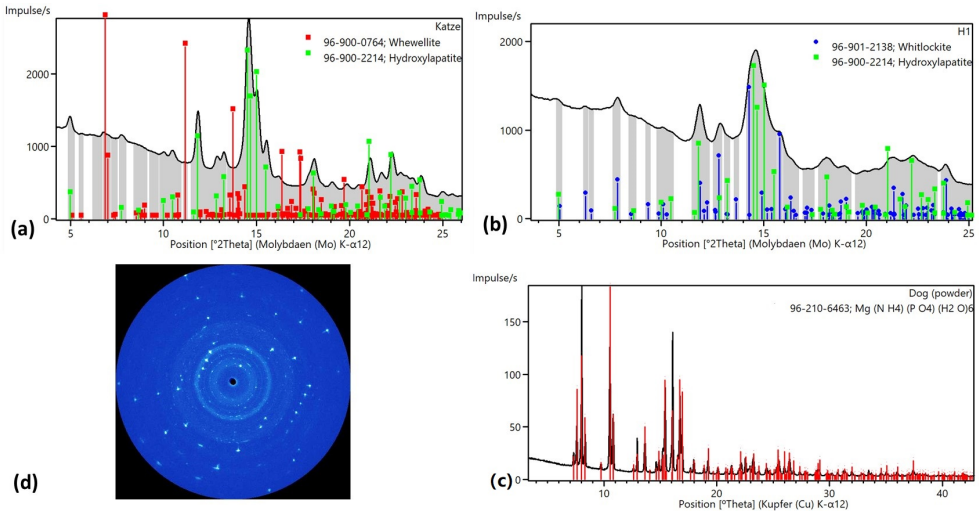

Figure A1. Detailed phase analysis of three urinary stones. XRD 1D profiles of stones from (**a**) a cat, (**b**) a human, and (**c**) a dog. (**d**) A 2D diffraction image with the high-intensity dots showing the single crystallinity.

References

1. Straub, M.; Hautmann, R. Urolithiasis-Harnsteinerkrankung. In *Urologie*; Springer: Berlin/Heidelberg, Germany, 2010; pp. 269–302. [CrossRef]
2. Green, W.; Ratan, H. Molecular mechanisms of urolithiasis. *Urology* **2013**, *81*, 701–704. [CrossRef] [PubMed]
3. Hidas, G.; Eliahou, R.; Duvdevani, M.; Coulon, P.; Lemaitre, L.; Gofrit, O.N.; Pode, D.; Sosna, J. Determination of renal stone composition with dual-energy CT: In vivo analysis and comparison with x-ray diffraction. *Radiology* **2010**, *257*, 394–401. [CrossRef] [PubMed]
4. Liu, Y.; Qu, M.; Carter, R.E.; Leng, S.; Ramirez-Giraldo, J.C.; Jaramillo, G.; Krambeck, A.E.; Lieske, J.C.; Vrtiska, T.J.; McCollough, C.H. Differentiating Calcium Oxalate and Hydroxyapatite Stones InVivo Using Dual-Energy CT and Urine Supersaturation and pH Values. *Acad. Radiol.* **2013**, *20*, 1521–1525. [CrossRef] [PubMed]
5. McCarthy, C.J.; Baliyan, V.; Kordbacheh, H.; Sajjad, Z.; Sahani, D.; Kambadakone, A. Radiology of renal stone disease. *Int. J. Surg.* **2016**, *36*, 638–646. [CrossRef]
6. Brisbane, W.; Bailey, M.R.; Sorensen, M.D. An overview of kidney stone imaging techniques. *Nat. Rev. Urol.* **2016**, *13*, 654–662. [CrossRef]
7. Qu, M.; Ramirez-Giraldo, J.C.; Leng, S.; Williams, J.C.; Vrtiska, T.J.; Lieske, J.C.; McCollough, C.H. Dual-energy dual-source CT with additional spectral filtration can improve the differentiation of non-uric acid renal stones: An ex vivo phantom study. *Am. J. Roentgenol.* **2011**, *196*, 1279–1287. [CrossRef]
8. Tao, S.; He, C.; Hao, X.; Kuang, C.; Liu, X. Principles of different x-ray phase-contrast imaging: A review. *Appl. Sci.* **2021**, *11*. [CrossRef]
9. Wilkins, S.W.; Nesterets, Y.I.; Gureyev, T.E.; Mayo, S.C.; Pogany, A.; Stevenson, A.W. On the evolution and relative merits of hard X-ray phase-contrast imaging methods. *Philos. Trans. R. Soc. A Math. Phys. Eng. Sci.* **2014**, *372*. [CrossRef]
10. Yashiro, W.; Terui, Y.; Kawabata, K.; Momose, A. On the origin of visibility contrast in x-ray Talbot interferometry. *Opt. Express* **2010**, *18*, 16890. [CrossRef]
11. Strobl, M. General solution for quantitative dark-field contrast imaging with grating interferometers. *Sci. Rep.* **2014**, *4*, 7243. [CrossRef]
12. Graetz, J.; Balles, A.; Hanke, R.; Zabler, S. Review and experimental verification of X-ray dark-field signal interpretations with respect to quantitative isotropic and anisotropic dark-field computed tomography. *Phys. Med. Biol.* **2020**, *65*, 235017. [CrossRef] [PubMed]
13. Ando, M.; Gupta, R.; Iwakoshi, A.; Kim, J.K.; Shimao, D.; Sugiyama, H.; Sunaguchi, N.; Yuasa, T.; Ichihara, S. X-ray dark-field phase-contrast imaging: Origins of the concept to practical implementation and applications. *Phys. Med.* **2020**, *79*, 188–208. [CrossRef] [PubMed]
14. Mayo, S.C.; Stevenson, A.W.; Wilkins, S.W. In-Line Phase-Contrast X-ray Imaging and Tomography for Materials Science. *Materials* **2012**, *5*, 937–965. [CrossRef] [PubMed]
15. Hudspeth, M.; Claus, B.; Dubelman, S.; Black, J.; Mondal, A.; Parab, N.; Funnell, C.; Hai, F.; Qi, M.L.; Fezzaa, K.; et al. High speed synchrotron x-ray phase contrast imaging of dynamic material response to split Hopkinson bar loading. *Rev. Sci. Instrum.* **2013**, *84*. [CrossRef]

16. Saghamanesh, S.; Griffa, M.; Zboray, R. X-ray speckle-based dark-field imaging of water transport in porous ceramics. In Proceedings of the International Conference on Industrial Computed Tomography, Wels, Austria, 8–11 February 2022; pp. 11–16.
17. Gao, J.; Kedir, N.; Kirk, C.D.; Hernandez, J.; Wang, J.; Paulson, S.; Zhai, X.; Horn, T.; Kim, G.; Gao, J.; et al. Real-time damage characterization for GFRCs using high-speed synchrotron X-ray phase contrast imaging. *Compos. Part B Eng.* **2021**, *207*, 108565. [CrossRef]
18. Nielsen, M.S.; Lauridsen, T.; Christensen, L.B.; Feidenhans'l, R. X-ray dark-field imaging for detection of foreign bodies in food. *Food Control* **2013**, *30*, 531–535. [CrossRef]
19. Massimi, L.; Suaris, T.; Hagen, C.K.; Endrizzi, M.; Munro, P.R.T.; Havariyoun, G.; Hawker, P.M.S.; Smit, B.; Astolfo, A.; Larkin, O.J.; et al. Volumetric high-resolution X-ray phase-contrast virtual histology of breast specimens with a compact laboratory system. *IEEE Trans. Med. Imaging* **2021**. [CrossRef]
20. Saghamanesh, S.; Dimitriu LaGrange, D.; Reymond, P.; Wanke, I.; Lövblad, K.O.; Neels, A.; Zboray, R. Non contrast enhanced volumetric histology of blood clots through high resolution propagation-based X-ray microtomography. *Sci. Rep.* **2022**, *12*, 2778. [CrossRef]
21. Romano, M.; Bravin, A.; Wright, M.D.; Jacques, L.; Miettinen, A.; Hlushchuk, R.; Dinkel, J.; Bartzsch, S.; Laissue, J.A.; Djonov, V.; et al. X-Ray Phase Contrast 3D Virtual Histology: Evaluation of Lung Alterations After Microbeam Irradiation. *Int. J. Radiat. Oncol. Biol. Phys.* **2022**, *112*, 818–830. [CrossRef]
22. Eckermann, M.; Schmitzer, B.; Van der Meer, F.; Franz, J.; Hansen, O.; Stadelmann, C.; Salditt, T. Three-dimensional virtual histology of the human hippocampus based on phase-contrast computed tomography. *Proc. Natl. Acad. Sci. USA* **2021**, *118*, 1–12. [CrossRef]
23. Zdora, M.C.; Thibault, P.; Kuo, W.; Fernandez, V.; Deyhle, H.; Vila-Comamala, J.; Olbinado, M.P.; Rack, A.; Lackie, P.M.; Katsamenis, O.L.; et al. X-ray phase tomography with near-field speckles for three-dimensional virtual histology. *Optica* **2020**, *7*, 1221. [CrossRef]
24. Chourrout, M.; Rositi, H.; Ong, E.; Hubert, V.; Paccalet, A.; Foucault, L.; Autret, A.; Fayard, B.; Olivier, C.; Bolbos, R.; et al. Brain virtual histology with X-rayphase-contrast tomographyPart I: Whole-brain myelin mapping in white-matter injury models. *Biomed. Opt. Express* **2021**. [CrossRef]
25. Horng, A.; Stroebel, J.; Geith, T.; Milz, S.; Pacureanu, A.; Yang, Y.; Cloetens, P.; Lovric, G.; Mittone, A.; Bravin, A.; et al. Multiscale X-ray phase contrast imaging of human cartilage for investigating osteoarthritis formation. *J. Biomed. Sci.* **2021**, *28*, 1–14. [CrossRef] [PubMed]
26. Momose, A. X-ray phase imaging reaching clinical uses. *Phys. Med.* **2020**, *79*, 93–102. [CrossRef] [PubMed]
27. Bravin, A.; Coan, P.; Suortti, P. X-ray phase-contrast imaging: From pre-clinical applications towards clinics. *Phys. Med. Biol.* **2013**, *58*, R1-35 [CrossRef]
28. Gureyev, T.E.; Mayo, S.C.; Myers, D.E.; Nesterets, Y.; Paganin, D.M.; Pogany, A.; Stevenson, A.W.; Wilkins, S.W. Refracting Röntgen's rays: Propagation-based x-ray phase contrast for biomedical imaging. *J. Appl. Phys.* **2009**, *105*. [CrossRef]
29. Pfeiffer, F.; Bech, M.; Bunk, O.; Kraft, P.; Eikenberry, E.F.; Brönnimann, C.; Grünzweig, C.; David, C. Hard-X-ray dark-field imaging using a grating interferometer. *Nat. Mater.* **2008**, *7*, 134–137. [CrossRef]
30. Olivo, A.; Speller, R. Image formation principles in coded-aperture based x-ray phase contrast imaging. *Phys. Med. Biol.* **2008**, *53*, 6461–6474. [CrossRef]
31. Morgan, K.S.; Paganin, D.M.; Siu, K.K. X-ray phase imaging with a paper analyzer. *Appl. Phys. Lett.* **2012**, *100*. [CrossRef]
32. Bérujon, S.; Ziegler, E.; Cerbino, R.; Peverini, L. Two-Dimensional X-Ray Beam Phase Sensing. *Phys. Rev. Lett.* **2012**, *108*, 158102. [CrossRef]
33. Scherer, K.; Braig, E.; Willer, K.; Willner, M.; Fingerle, A.A.; Chabior, M.; Herzen, J.; Eiber, M.; Haller, B.; Straub, M.; et al. Non-invasive Differentiation of Kidney Stone Types using X-ray Dark-Field Radiography. *Sci. Rep.* **2015**, *5*, 9527. [CrossRef] [PubMed]
34. Lauridsen, T.; Willner, M.; Bech, M.; Pfeiffer, F.; Feidenhans'l, R. Detection of sub-pixel fractures in X-ray dark-field tomography. *Appl. Phys. A* **2015**, *121*, 1243–1250. [CrossRef]
35. Hu, S.; Yang, F.; Griffa, M.; Kaufmann, R.; Anton, G.; Maier, A.; Riess, C. Towards quantification of kidney stones using X-ray dark-field tomography. In Proceedings of the 2017 IEEE 14th International Symposium on Biomedical Imaging (ISBI 2017), Melbourne, VIC, Australia, 18–21 April 2017; pp. 1112–1115.
36. Saghamanesh, S.; Aghamiri, S.M.R.; Olivo, A.; Sadeghilarijani, M.; Kato, H.; Kamali-Asl, A.; Yashiro, W. Edge-illumination X-ray phase contrast imaging with Pt-based metallic glass masks. *Rev. Sci. Instrum.* **2017**, *88*, 063705. [CrossRef] [PubMed]
37. Zdora, M.C. State of the Art of X-ray Speckle-Based Phase-Contrast and Dark-Field Imaging. *J. Imaging* **2018**, *4*, 60. [CrossRef]
38. Saghamanesh, S.; Zboray, R. Virtual speckle-based X-ray phase-contrast and dark-field imaging with digital phantoms. *Opt. Express* **2021**, *29*, 41703. [CrossRef]
39. Berujon, S.; Ziegler, E. Near-field speckle-scanning-based X-ray tomography. *Phys. Rev. A* **2017**, *95*, 1–8. [CrossRef]
40. Pavlov, K.M.; Li, H.T.; Paganin, D.M.; Berujon, S.; Rougé-Labriet, H.; Brun, E. Single-Shot X-Ray Speckle-Based Imaging of a Single-Material Object. *Phys. Rev. Appl.* **2020**, *13*, 054023. [CrossRef]
41. Degen, T.; Sadki, M.; Bron, E.; König, U.; Nénert, G. The HighScore suite. *Powder Diffr.* **2014**, *29*, S13–S18. [CrossRef]